In–line phase contrast breast tomosynthesis: A phantom feasibility study at a synchrotron radiation facility

K. Bliznakova[1], P. Russo[2], Z. Kamarianakis[4], G. Mettivier[2], H. Requardt[3], A. Bravin[3], and I. Buliev[1]

[1]Department of Electronics, Technical University of Varna, 1 Studentska Str, Varna, 9010 Bulgaria

[2]Dipartimento di Fisica, Università di Napoli Federico II, and INFN Sezione di Napoli, Via Cintia, I-80126, Naples, Italy

[3]European Synchrotron Radiation Facility (ESRF), Grenoble F-38043, France

[4]Department of Medical Physics, University of Patras, 26500, Greece

Corresponding Author:

Kristina Bliznakova:
Tel: +359 52 383 619
e-mail: kristina.bliznakova@tu-varna.bg

Abstract

Purpose: The major objective is to adopt, apply and test developed in-house algorithms for volumetric breast reconstructions from projection images, obtained in in-line phase contrast mode.

Methods: Four angular sets, each consisting of 17 projection images obtained from four physical phantoms were acquired at beamline ID17, ESRF, Grenoble, France. The tomosynthesis arc was ±32º. The physical phantoms differed in the complexity of the texture and introduced features of interest. Three of the used phantoms were in-house developed, made of epoxy resin, polymethyl-methacrylate (PMMA) and paraffin wax, while the fourth phantom was the CIRS BR3D. Projection images were with pixel size of 47 µm x 47 µm. Tomosynthesis images were reconstructed with standard shift and add (SAA) and filtered backprojection (FBP) algorithms.

Results: It was found that edge-enhancement observed in planar x-ray images is preserved in tomosynthesis images from both phantoms with homogeneous and highly heterogeneous backgrounds. In case of BR3D, it was found that features not visible in the planar case were well outlined in tomosynthesis slices. In addition, the edge enhancement index calculated for features of interest was found out much higher in tomosynthesis images reconstructed with FBP in comparison to planar images and tomosynthesis images reconstructed with SAA. The comparison between images reconstructed by the two reconstruction algorithms shows an advantage for the FBP method in terms of better edge enhancement.

Conclusions: Phase contrast breast tomosynthesis realized in in-line mode benefits the detection of suspicious areas in mammography images by adding the edge enhancement effect to the reconstructed slices.

Keywords: Breast tomosynthesis, Phase contrast imaging, Phase contrast tomosynthesis, Inhomogeneous background

I. Introduction

Digital Breast Tomosynthesis (DBT) is a promising three-dimensional (3D) x-ray imaging modality already in daily clinical practice for breast cancer screening (Sechopoulos, 2013). Several studies have shown that the addition of DBT to digital mammography is associated with a decrease in recall rate and an increase in cancer detection rate (Durand *et al.*, 2015; Friedewald *et al.*, 2014). The technique allows to partially remove the influence of overlapping tissues, which is intrinsic to two-dimensional (2D) mammography and may lead to improved breast cancer visualisation. Typically, DBT uses 9 to 25 projection images of the breast acquired with dedicated x-ray based mammography systems. The spatial resolution of DBT is in the order of 0.1mm×0.1mm×1mm (x×y×z), whereas digital mammography has a resolution in the order of 0.1mm×0.1mm×50mm. Each projection image requires only a fraction of the total dose of a full 2D mammogram because all of the projection images are added together to synthesize the tomographic planes (Kopans, 2014).

While cone beam breast CT with dedicated scanners is a fully 3D technique for breast imaging, which produces isotropic resolution (Sarno *et al.*, 2015), in DBT the various views are input to reconstruction algorithms to provide a pseudo 3D image of the breast. However, DBT (as well as breast CT) is based on projections acquired in absorption mode, where x-ray images are formed from the local variations in the absorption properties of the various breast tissues. In this imaging modality, the tumour contrast in projection images (with respect to background fibroglandular tissue) is less than 10%, typically, since the values of the x-ray attenuation coefficient $\mu(E)$ of normal (fibroglandular) and cancerous breast structures (like invasive / non-invasive ductal and lobular carcinoma) differ by only few percent at most, in the photon energy range from 15 keV to 110 keV.

One approach to increase tumour and microcalcification contrast in tomosynthesis images is by using Phase Contrast (PhC) projection images in the tomosynthesis setup instead of images acquired in attenuation mode. Grating-based PhC and in-line PhC experimental arrangements were recently reported as approaches that may be used to produce PhC images. In the case of grating-based PhC tomosynthesis, Schleede et al. (Schleede *et al.*, 2014) presented for the first time results from a tomosynthesis of a 9-mm thick mastectomy sample section characterised by an invasive ductal carcinoma. PhC tomosynthesis slices showed improved visibility of fibrous structures in comparison to absorption based tomosynthesis; moreover, some tissue structures were visible only in PhC tomosynthesis images. In the same line of research, Li et al. (Li *et al.*, 2014) reported on a PhC tomosynthesis study realised with twenty one projection images obtained for each of the three in-house developed physical objects with known $\mu(E)$ and $\delta(E)$ characteristics. Both the filtered backprojection method (FBP) realized with a Hilbert kernel and a shift-and-add algorithm (SAA), were used as reconstruction algorithms. They concluded that neither of the reconstruction methods, applied in their studies, can be used to replace the absorption based tomosynthesis. Moreover, the authors suggested that absorption and PhC mechanisms provide complementary information. Another study, reported by Szafraniec et al. (Szafraniec *et al.*,

2014) showed that strong PhC signal is preserved in tomosynthesis images obtained from a "double TORMAM" phantom with a total thickness of 3.2 cm in their coded-aperture based laboratory implementation of x-ray PhC tomosynthesis. Phantom details of interest were clearly isolated, while a strong PhC signal was preserved at the edges of details in tomosynthesis images, reconstructed by an iterative algorithm. The studies of Li *et al.* and Szafraniec *et al.* however, concerned phantoms with a homogeneous background.

In-line (or propagation based) implementation of PhC tomosynthesis has been also reported (Ikeya *et al.*, 2013; Hammonds *et al.*, 2011; Guan *et al.*, 2014a). In this technique, no optical elements like apertures or gratings are used in the beam path for x-ray acquisitions. Arrangements included experimental systems either in laboratory or at synchrotron facilities, and polymethyl methacrylate (PMMA) phantoms with features of interest imaged in PhC tomosynthesis conditions. Reconstruction algorithms used in these studies were FBP and SAA. The PhC tomosynthesis images retained the edge enhancement effects observed in the planar projection images of simple PMMA phantoms. More recently, Guan et al. (Guan *et al.*, 2014b) showed through simulations that x-ray PhC tomosynthesis provides better *z*-resolution than conventional DBT. The authors used an advanced iterative algorithm with PhC images simulated within an angular arc of 40º.

These preliminary studies, although carried out with simple phantoms, point out the potential benefits of applying x-ray PhC tomosynthesis for imaging the breast, in the simple geometry of in-line PhC imaging. They also motivate further development and optimisation of this technique as well as its clinical application towards successful detection of suspicious regions in mammography images and better differentiation of breast structures. The use of more complex and thicker phantoms is necessary for this purpose.

In this work the authors adopt, apply and test in-house developed algorithms for volumetric breast reconstructions from PhC projection images, obtained in an in-line PhC tomosynthesis setup. The investigative goal is to test whether enhanced edges of image details (including breast-like lesions) – produced by phase contrast with a highly coherent, monochromatic x-ray source – are preserved in tomosynthesis reconstructed images of phantoms characterized by different structural complexity. The specific objectives of the study are: (a) to demonstrate the ability to synthesize tomosynthesis images of various in complexity phantoms, which are built from materials some of them having characteristics close to the absorption and the refractive characteristics of real breast tissue using PhC setup at synchrotron facility; (b) to apply and compare in-house developed 3D algorithms for reconstruction of PhC tomosynthesis slice images devised for x-ray breast imaging; (c) to evaluate the amount of the edge enhancement effects in PhC tomosynthesis images for the tested reconstruction algorithms.

Experiments were carried out at the European Synchrotron Radiation Facility (ESRF) (Grenoble, France) using four physical phantoms made of materials commonly utilized in the construction of phantoms in x-ray diagnostic imaging. PhC tomosynthesis was implemented by acquiring 17 angular views of these phantoms within an angular span of $\pm32^0$; tomosynthesis slices were reconstructed by the standard SAA and FPB algorithms.

Furthermore, reconstructed slices were compared to the corresponding planar images in terms of feature visibility and sharpness.

II. Materials and Methods

II.A. Phantoms

Four physical phantoms of various composition and complexity were used in the study (Fig. 1): *(a) PMMA phantom* (phantom 1) - a homogeneous PMMA sample in the form of a slab of size 6cm×6cm×4cm in which four air-filled cylindrical holes (diameter of 1 mm) were drilled vertically to its smallest face; (b) *Paraffin phantom* (phantom 2) - a homogenous paraffin slab of size 6cm ×4 cm × 2.5cm, containing three water spheres (diameter of 0.8 cm), placed at different depths in the slab; (c) *Epoxy resin phantom with air bubbles* (phantom 3) - a rectangular polystyrene flask with size 6cm ×4 cm× 2 cm filled with an epoxy resin mixture and then shacked in order to produce a large number of air sacs of different size; (d) *CIRS model 020 BR3D* (phantom 4) - five slabs stacked together to simulate a 5-cm thick compressed breast with tissue composition of 50% glandular - 50% adipose (CIRS). The central slab of the stack contains details simulating microcalcifications, fibers and masses.
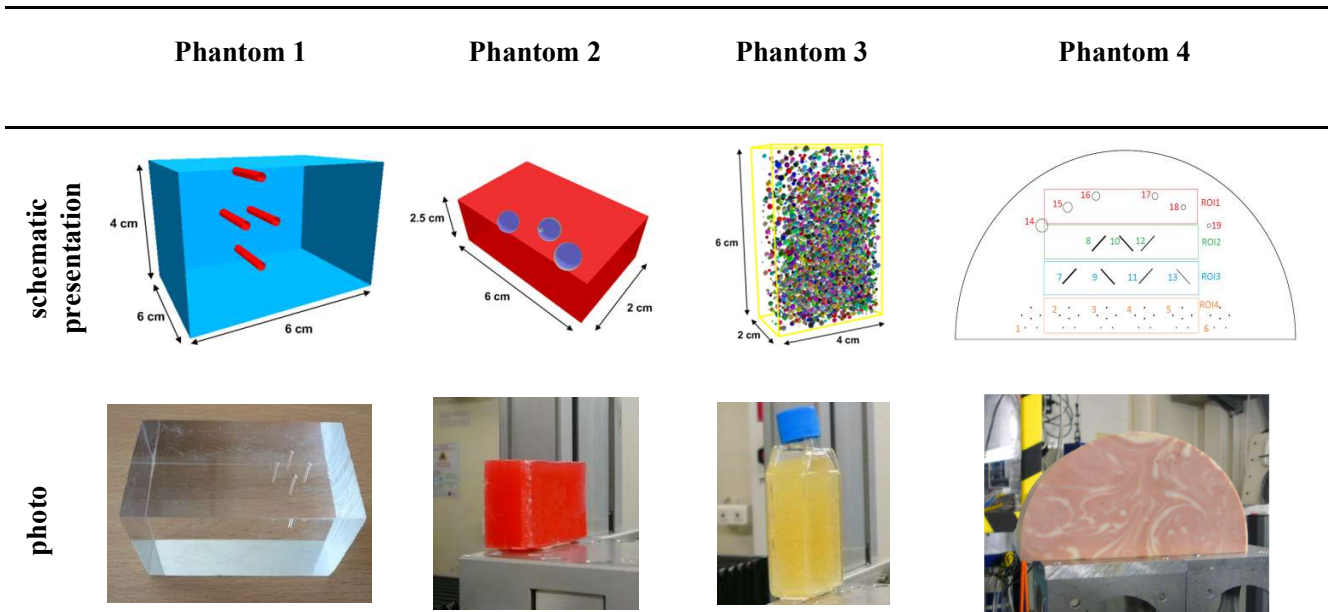
| Phantom 1 | Phantom 2 | Phantom 3 | Phantom 4 |

Figure 1: Phantoms used in the experimental study. Phantoms 1 and 2 are homogeneous slabs embedding test objects inserted at different positions as shown in the first row. They were used for initial evaluation of the reconstruction algorithms. Phantoms 3 and 4 represent complex phantoms dedicated to test the performance of PhC tomosynthesis with objects characterised by an inhomogeneous texture. The ROIs under investigation for phantom 4 are noted on its schematic presentation as ROI1 to ROI4.

The first row in figure 1 shows a schematic representation of the phantoms, used in this study, while the second row shows photos of the physical phantoms used in the experimental work, respectively. The linear attenuation coefficients and the refractive indexes of the materials used in the experimental work are summarised in table 1. For comparison purposes, we provide the corresponding coefficients for breast tissues as well.

Table 1. Elemental composition as percentage weights, density, linear attenuation coefficient and refractive index decrement of materials used in the study for 35keV.

Material	Composition	Density, g cm^{-3}	Linear Attenuation Coefficient, μ cm^{-1}	Refractive Index, δ
PMMA*	H: 0.080; C: 0.600; O: 0.320	1.19	0.31	2.18 x 10^{-7}
Paraffin	H 0.150; C: 0.850	0.93	0.23	1.81 x 10^{-7}
Epoxy resin	H: 0.070; C: 0.740; O: 0.190	1.10	0.31	2.45 x 10^{-7}
H$_2$O*	H: 0.110; O: 0.890	1.00	0.31	1.88 x 10^{-7}
Adipose*	H: 0.119; C:0.637; N:0.008; O:0.232; Na:0.001; P:0.0002 S:0.0007; Cl:0.001; K:0.0003	0.92	0.24	1.75 x 10^{-7}
Gland*	H: 0.106; C: 0.332; N: 0.030; O: 0.527; Na: 0.001; P: 0.001 S: 0.002; Cl: 0.001	1.02	0.31	1.94 x 10^{-7}

$*$ Data taken from CSIRO Imaging portal (https://www.ts-imaging.net/Default.aspx)

The refractive index decrements (δ) for four of the materials in table 1 were taken from the CSIRO Imaging portal. The refractive index decrement for the rest of the materials is calculated by taking into account that $\delta = N_e*(r_e \lambda^2)/2\pi$, where r_e is the classical electron radius, while N_e is the electron density of the tissue and λ is the wavelength. For each element and composition, N_e is calculated, knowing the chemical formula for each material simulated. Linear attenuation coefficients for these materials were taken from XCOM database (Berger *et al.*, 2010).

II. B. Experimental Setup

The experiment was conducted at the biomedical beamline ID17 at ESRF (Bravin *et al.*, 2007). The coherent radiation is obtained from the wigglers of the storage ring. A monolithic channel-cut Si (111) crystal is placed 153 m from the source to produce a monochromatic beam, with energy selectable in the range 25–140 keV. A tungsten slit system, located approximately 150 m from the source, collimated the beam cross section to a size of 150 mm× 6 mm; the photon energy for the experiments was 35 keV.

The detector was a tapered optics FReLoN 2k CCD camera, a fast readout and low noise charge coupled device with a pixel size of 47 μm and a field-of-view 95×95 mm^2. It was located at a distance of 11 m downstream of the beam exit surface of the phantom. Further, the FReLoN camera was placed on a fixed platform and the phantoms were mounted horizontally on a motorized scanning stage that could rotate around a vertical axis and translate vertically. Images for tomosynthesis were obtained by the following setup. Each phantom was scanned by rotating the phantom stage in a full arc of 360^0 and projection views were recorded every 4^0. From the whole set of 90 images, 17 projection images were used for tomosynthesis, in an arc from -32^0 to $+32^0$, where 0^0 is the direction normal to one of the largest faces of the phantom slab. Due to the limited vertical extent of the beam (6 mm), in order to scan the whole height of the phantom its supporting platform was translated vertically at the end of each full rotation, in a rotate-translate sequence. Depending on the phantom's height, the number of vertical scans varied. The size of the recorded images was 2048 (width) $\times$ 93 (height) pixels. The whole projection image was then obtained by combining the different images acquired in a single vertical step; for phantom 1, the image size was 2048×1003 pixels, for phantom 2: 2048×1062 pixels, for phantom 3: 2048×236 pixels and for phantom 4: 2048×2242 pixels. The incident air kerma per single projection image was 0.33 mGy, while the exposure duration time was 26ms.

II. C. Projection data processing and reconstruction algorithms used

Tomosynthesis images were reconstructed with an in-house developed reconstruction platform (Kamarianakis *et al.*, 2014). The PIRXI software platform (Platform for Image Reconstruction in X-ray Imaging) is a tool based on the RTCL: Reconstruction Techniques Class Library, which is another in-house developed object-oriented library for x-ray based applications (Kamarianakis *et al.*, 2013). This platform permits fast development of known image reconstruction algorithms based on various projection data from known image acquisition setups (e.g. CT, tomosynthesis, etc.) and programming and testing of new reconstruction techniques, using modified or new projection acquisition trajectories. The core components of the platform are C++ classes that provide the user with software equivalents of a real CT imaging chain (e.g. x-ray source, flat-panel detector, image reconstruction processor, etc). By combining instances of these classes with the appropriate methods on projection data (e.g. filtering, 3D transformations) the user can repeat and simulate a large variety of imaging setup and eventually use the processed images to reconstruct objects at arbitrary orientations.

Two basic algorithms: the SAA and the FBP algorithm are fully implemented in the platform. Both line integrals and x-ray intensity images can be used to reconstruct tomograms. Different types of filters may be selected for the FBP algorithm. The geometry may be isocentric rotational and partially isocentric (stationary detector). The parameters adjusted for the algorithms to reconstruct tomograms from phase contrast projections mainly concerned the geometry (rotating object, stable source and detector), as the deviation and the actual position of the detector with respect to the axis of the object rotation was accurately identified from the acquired projection images and taken into account in the reconstructions.

For the purposes of this study, the size of the in-plane reconstructed voxel size was set to 43.6μm x 43.6μm. The voxels were considered anisotropic, by means of the slice separation. Slice thickness was set to 0.1 mm. Images were reconstructed with both SAA and FBP algorithms. Advanced iterative techniques were not considered at this stage. A detailed comparison and optimisation of algorithms, including iterative-based methods will be performed in the follow up experimental and simulation study on tomosynthesis images of anthropomorphic breast phantoms with known realistic breast tissue distribution. In case of FBP, prior to reconstruction, projection images were pre-processed with a modified ramp filter kernel. The required Ram-Lak filter was combined with an apodization window to suppress the highest frequency components and reduce the influence of the random noise while keeping an optimal spatial resolution loss. No other pre-processing (e.g. denoising methods) was applied prior to backprojection in all cases. The reconstructed set of images varied from 400 slices for phantoms 1 and 2, to 500 slices for phantoms 3 and 4 in order to cover the volumes of interest.

II. D. Evaluation of image quality

To quantify differences in the conspicuity of the edge-enhancement effect of objects in reconstructed and projection images, the edge-enhancement index (EEI) and the edge enhancement to noise ratio (EE/N) adopted by Donnelly *et al. (Donnelly et al., 2006)* were used:

$$EEI = \frac{(P-T)/(P+T)}{(H-L)/(H+L)} \qquad\qquad EE/N = \frac{P-T}{\sqrt{\sigma_H{}^2 + \sigma_L{}^2}}$$

where P and T are the peak and the trough intensity value at the edge, respectively; H and L are the intensity values that would result at these locations if there were no edge enhancement at the high and the low intensity regions next to the edge. H and L values were calculated for a square region of size 100 x 100 pixels near the corresponding edge. σ_H and σ_L represent the standard deviation of the pixels in the region of interest used to calculate H and L values, respectively. The first metric, the EEI, was used to quantify the edge enhancement effect relative to the absolute change in intensity from absorption differences across the edge, while the second metric, EE/N, was utilised to quantify the enhancement relatively to the image noise.

In addition to the quantitative assessment, a task-based evaluation was designed for the images which belong to the experiment with the CIRS model 020 BR3D. The study included three radiologists with more than 10 years experience in the field of radiology and 17 slides with images representing regions of interest extracted from a planar image and reconstructed images with FBP and SAA. The first slide contained the schematic image of phantom 4 with the four regions of interest. It is followed by four slides per ROI: ROI reconstructed by FBP, ROI reconstructed by SAA, planar ROI, and a slide containing all three ROIs.

In the case of masses, the observers were told that there are four masses with different size. The observers were asked to estimate the number of masses they see for each modality. In addition, they were asked to use grades

from 1 to 5 for each of the masses: 1(clearly absent), 2(probably absent), 3(present or absent), 4(probably present), 5(clearly present). For the microcalcifications, the observers were told that in the images there exist six microcalcifications per group with different size. They were asked to estimate the number of microcalcifications they see for each group, as well as to evaluate their visibility by using scores between 1 and 5. Similar guides were given in respect to the nylon fibers with different size.

III. Results and Discussion

III.A. Phase contrast tomosynthesis with simple homogeneous objects (Phantom 1, 2).

III.A.1. PMMA phantom (phantom 1)

Figure 2 shows projection images of phantom 1, corresponding to the view at 0º, and figure 3 shows corresponding tomosynthesis images reconstructed from the 17 acquired projection images of phantom 1 with the two tomosynthesis algorithms, relatively to phantom sections containing the air channels.
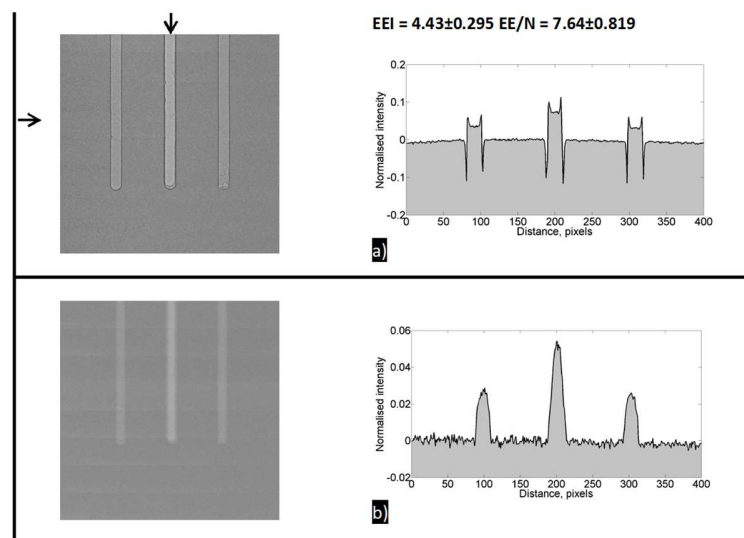

Figure 2: Projection images of the PMMA phantom with the four air filled cylindrical holes (phantom 1): a) projection image acquired in phase contrast arrangements (at 11 m distance); b) projection image acquired at object to detector distance of 17 cm. The short arrow at the top of the projection image in a) indicates the position of the two super-imposed cylindrical holes along the beam direction. The line profiles shown on the right side of each image are taken at a level in the image as shown by the arrow on the left side in image 2a.

The projection image shown in figure 2a is the image obtained at an object to detector distance of 11 m (where large PhC and edge enhancement effects are expected), while the image shown in figure 2b is the view obtained at an object to detector distance of 17 cm (where very low, or no, PhC and edge enhancement effects are expected due to the short propagation distance behind the object). Horizontal line profiles taken across these images are also shown. In both PhC and absorption projection images (figure 2a, b), there is a complete overlap of two of the air filled cylindrical holes embedded in the middle region of the phantom (see figure 1, phantom 1,

for which the x-ray beam enters from the top). By contrast, on tomosynthesis reconstructed slices (figure 3), all four air cavities are completely resolved and fully separated.
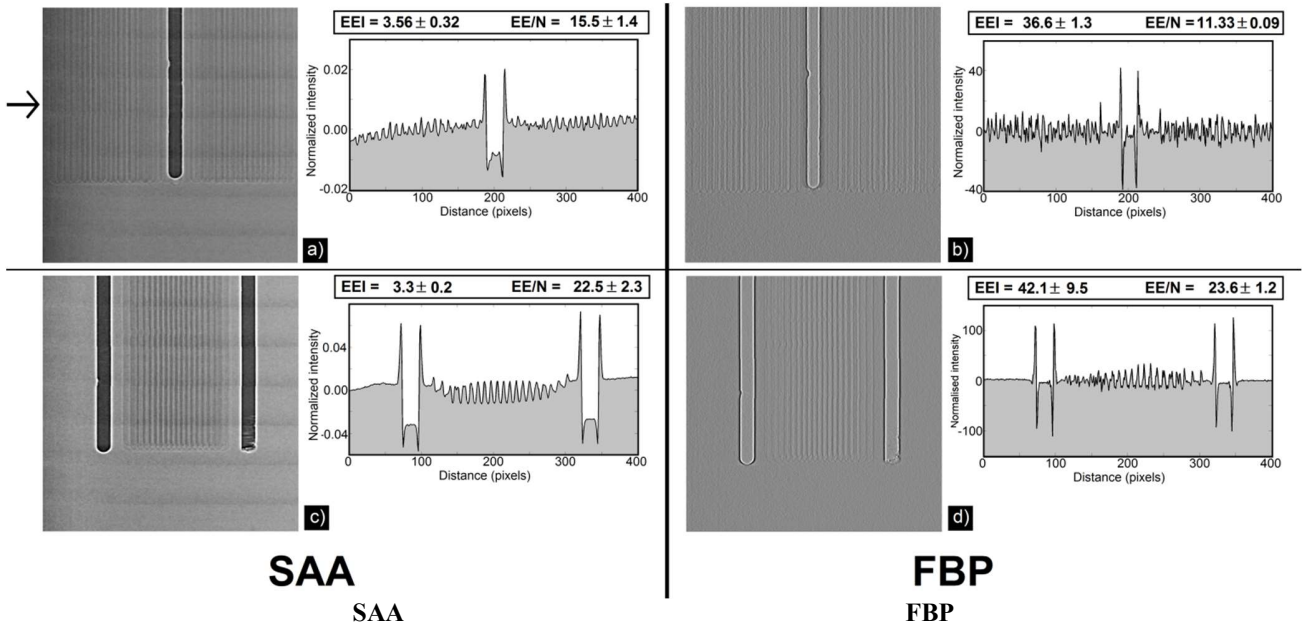

Figure 3: Tomosynthesis images (calculated from PhC projections), and corresponding horizontal line profiles (taken at a level as shown by the arrow on the left), of the PMMA phantom with the four air filled cylindrical holes (phantom 1): panels a) and c) show two reconstructed planes by using SAA, while panels b) and d) show the corresponding slices reconstructed by FBP algorithm. The planes are at heights in the phantom containing, one and two cylindrical holes in focus, respectively.

The reconstructed tomosynthesis images suffer from a strong artifact pattern, caused by the backprojected values of the edges of the out-of-plane phantom structures (for the used phantom these are the other cylinders and the phantom shape itself). This is a known effect, which in the case of PhC imaging is further enhanced. The nature of the artifacts is better presented in Figure 4, which shows an axial reconstruction slice through the four cylindrical holes. However, the tomosynthesis images have an obvious advantage compared to the planar images – despite the strong strike artifacts, one can clearly differentiate the four air filled cylinders and accurately determine their position in the PMMA phantom.
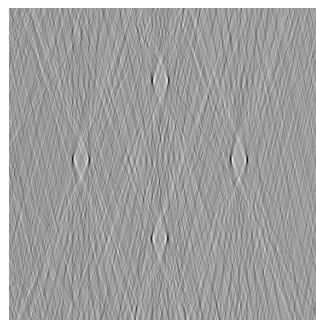

Figure 4: An axial slice taken through the all four cylinder holes.

The edge enhancement indexes and edge enhancement to noise ratios were calculated for each cylinder edge and subsequently these were averaged and shown at the top of the plot profiles. The edge enhancement effect, observed on the projection image in figure 2a, is fully preserved on all tomosynthesis images, and it is even more pronounced: the EEI in the projection image (figure 2a) is 4.43 and increases to 36.64 and 42.09 in the tomosynthesis slices reconstructed with the FBP algorithm, while the EEI for projection images and SAA tomosynthesis slices is similar. In case of SAA, the EEI is slightly reduced compared to the EEI calculated for the projection image, due to the weighting sum of the pixel values from the unfiltered projection images. In general, in tomosynthesis images obtained with SAA, the improved object edges from projections are preserved. The applied high-pass filter in the case of FBP further enhances the object edges leading to improved edge visibility and higher EEI in the tomosynthesis images.

Lowest noise values (the abbreviation N in EE/N) are obtained for the images reconstructed with SAA and for the planar projection images, while highest are calculated for FBP tomosynthesis slices. The latter mostly comes from the out-of-plane artifacts, which for the case of FBP are strongly pronounced, compared to SAA. However, due to the high EEI, the EE/N for SAA slices also retained at high levels: the EE/N index increases from 7.64 for the planar images (figure 2a) to 23.57 for the tomosynthesis image reconstructed with FBP (figure 3d). This EE/N improvement does also occur for the reconstructed with SAA image. In the case of SAA, the out-of plane edges are smeared which results in lower noise levels in the reconstructed images.

Similar results in terms of retained edge enhancement effects and EE/N improvement were claimed to be obtained by Hammonds *et al.* (Hammonds *et al.*, 2011) in their experimental work with a cylindrical phantom containing three holes drilled within it with a diameter of 2 mm, even though they used neither the SAA or the FBP algorithm but the multiple projection algorithm developed by Kolitsi *et al.* (Kolitsi *et al.*, 1992). The comparison of the two reconstruction algorithms SAA and FBP shown in figure 3 indicates an increased contrast of the reconstructed objects (in terms of EEI) for the FBP and reduced noise influence in tomosynthesis slices reconstructed by both algorithms (in terms of EE/N). Szafraniec *et al.* (Szafraniec *et al.*, 2014) also found that their edge-illumination PhC tomosynthesis setup preserved the edge enhancement observed in planar images even though the effect was not expressed in quantitative terms.

III.A.2. Paraffin phantom (phantom 2)

Figure 5a-d shows two reconstructed tomosynthesis slices from PhC projections of phantom 2 by using SAA (a, b) and FBP (c, d) algorithms. The selected slices are the central planes which pass through the middle (a, c) and leftmost (b, d) water spheres, respectively. The tomosynthesis slice in (b, d) is the central slice that passes through the leftmost sphere and at the same time corresponds to a slice that is 2mm away from the central slice that passes through the middle sphere (a, c). For comparison purposes, figure 5e and figure 5f show the projection images, which correspond to images of phantom 2 taken at 0º (central view) and object to detector

distances of 11 m and 17 cm, respectively. Line profiles taken across the spheres are shown in each sub-panel of figure 5. Similarly to the case of phantom 1, the edge enhancement indexes calculated for the edges of the central sphere (figure 5c, EEI = 91.43 and EE/N = 34.02) and of the left sphere (figure 5d, EEI = 50.76 and EE/N = 13.09) for the case of FBP were larger than the corresponding indexes calculated for these details in the PhC projection image (figure 5e, EEI = 11.10 and EE/N = 19.36), and tomosynthesis images obtained with SAA (figure 5a, EEI = 8.39 and EE/N = 19.20; figure 5b, EEI = 4.26 and EE/N = 12.61).
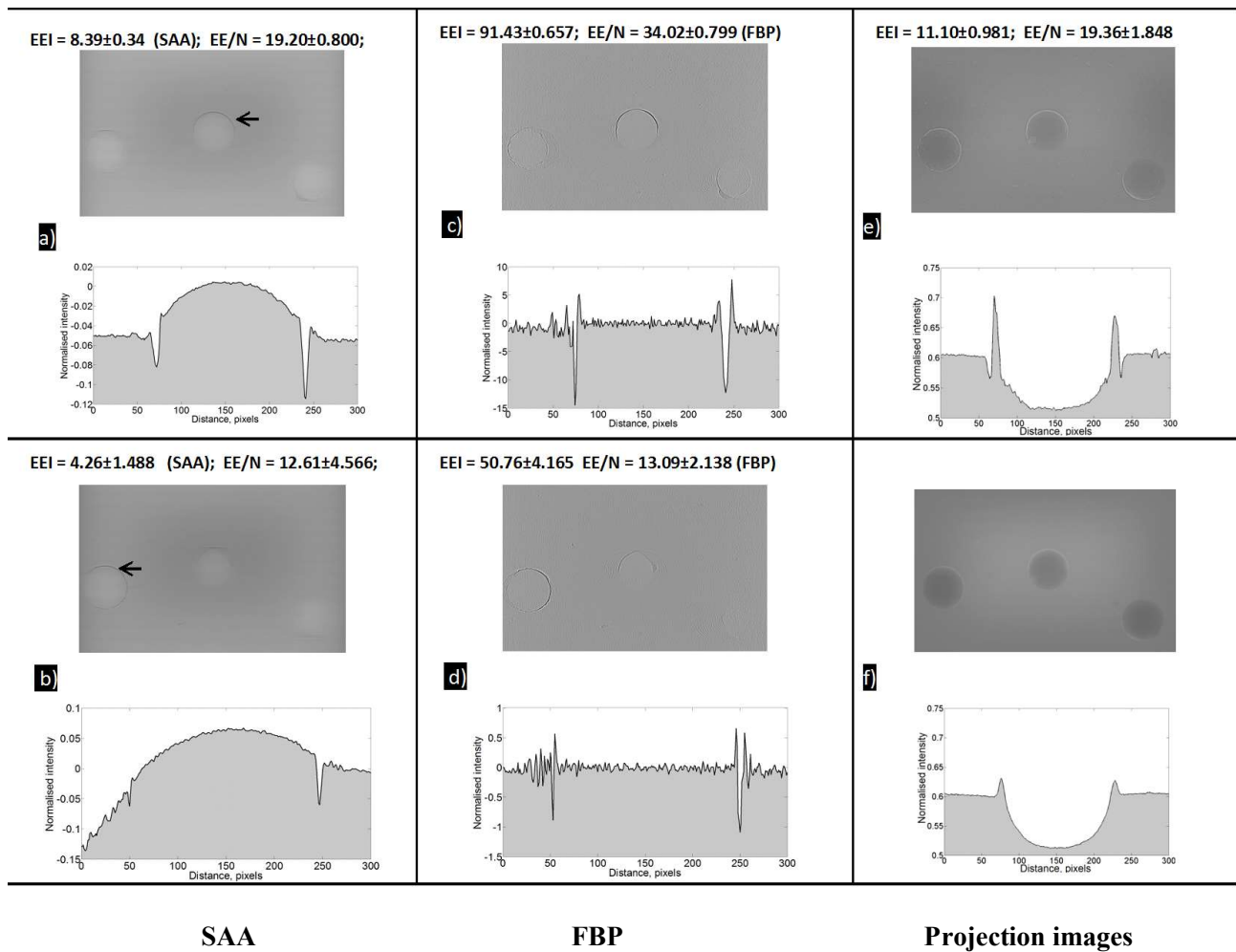

Figure 5: Comparison of reconstructed and planar images of the paraffin phantom (phantom 2). Selected reconstruction planes containing, respectively, the central (a, c) and the leftmost (b, d) of the three spheres embedded in this phantom; (e) projection image at 11 m distance from the detector and corresponding line profile; (f) projection image at 17 cm distance from the detector. Reconstruction planes are taken through the center of the spheres. Line profiles across the sphere are shown below each image in the panels. Images in (a, b) are reconstructed with SAA, while images in (c, d) are reconstructed with FBP algorithm. The arrows in images a) and b) shows the level at which the line profiles were taken.

This finding, and the similar results obtained in the previous section for the two experimental trials with simple phantoms incorporating homogeneous background, showed that the edge enhancement effect observed for features in PhC planar imaging is preserved, for the case of PhC tomosynthesis. The comparison between the two algorithms shows an advantage for the FBP approach in terms of better sharpness of the features' outline, as compared to the straightforward simple backprojection operation delivered by the SAA algorithm. This is also confirmed by the EEI and EE/N comparison between SAA and FBP images. The comparison shows that FBP results in higher EEI which objectively confirms the visually observed more enhanced objects edges in slices obtained by FBP compared to these obtained with SAA. This outcome is expected, in a certain degree, since the SAA uses unfiltered projection images.

The two algorithms can be applied using the same set of images. Each one of them provides a look on object slices in a different way: SAA better produces the flat regions and immediately reveals the different material regions. The flat regions still differ in the FBP reconstructions but in terms of mean intensity and to detect that difference, and additional low-pass filtering would be required. FBP strongly enhances any edges (their magnitude is in orders stronger, see figures 5a-d) and can be used to detect rather the borders between the different materials and this is especially useful for the detection of very small objects (as for example microcalcifications). Therefore, the authors consider the two algorithms as complementary, proving two different views without using additional radiation. Due to the limited scanning arc in tomosynthesis, the volumetric reconstructions suffer worse resolution in a direction perpendicular to the coronary planes (planes that are parallel to the detector) (Sechopoulos, 2013). The content presented on a coronary reconstruction image corresponds to a slice thicker than the pixels' width and height in the image and the thickness depends обратно пропорционално on the arc length. This is well seen in the axial reconstruction in Figure 4 (the coronary planes are parallel to the image lines and perpendicular to the image plane). Only the central reconstructed plane (the one that passes through its center) reveals the sphere as a circular object in the tomosynthesis images. This is illustrated in figures 5c and 5d, where one can observe the ovoid shape of the reconstructed sphere in a plane that is 2 mm away from the central plane for the case of the sphere in the middle of phantom 2. This is a known artifact for the tomosynthesis using circular scanning trajectory (Sarkar *et al.*, 2009) and it appears for the PhC tomosynthesis imaging, as well.

Nevertheless, to additionally confirm that, the authors simulated the experimental PhC imaging setup and using a computer model of the paraffin phantom (figure1, first row, second image), created PhC projection images and performed a series of CT and tomosynthesis reconstructions, following the methods adopted in a previous work (Bliznakova *et al.*, 2015). Coronal and axial reconstructions (by using FBP) are presented in figure 6.
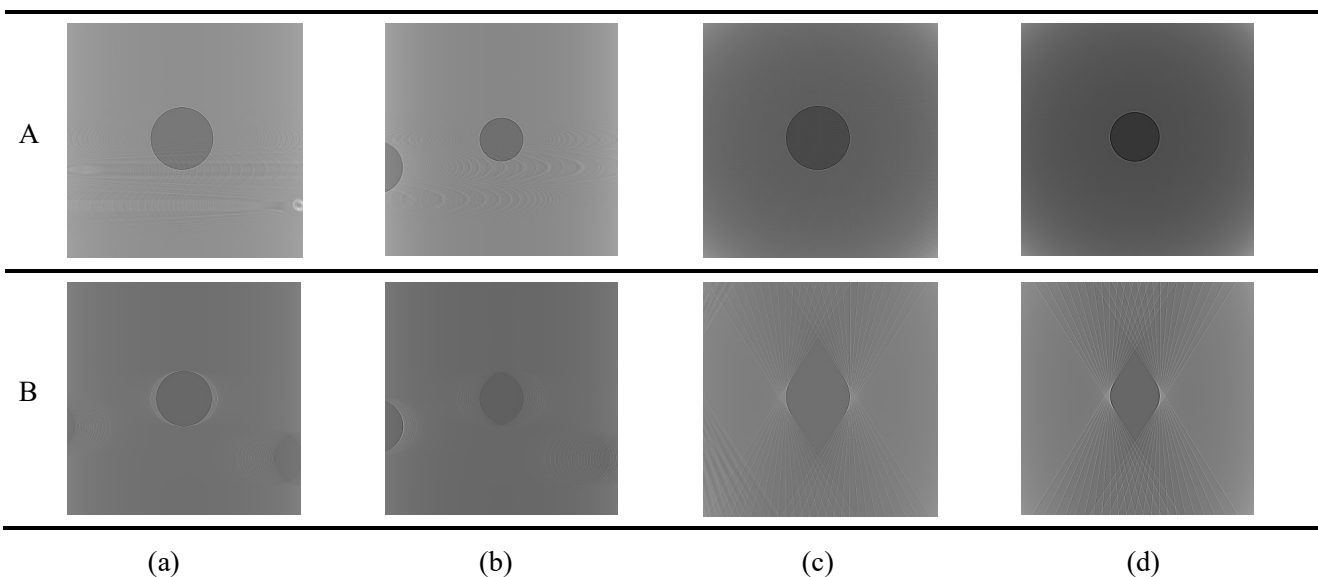
Figure 6: Comparison of (a-b) coronal and (c-d) axial reconstruction planes obtained from PhC projection images in (A) CT mode and (B) tomosynthesis mode at different depths in the reconstructed sphere: (a, c) – reconstructed slices correspond to the central plane of the spherical object, (b, d) reconstructed slices correspond to planes 2 mm away from the central plane. Inherent tomosynthesis artifacts are seen in images in (B).

The circular shape of the sphere cross-section is preserved in all reconstructed slices. The tomosynthesis images express the expected known artifacts.

III.B Phase contrast tomosynthesis with phantoms composed of inhomogeneous background

III.B.1. Epoxy phantom (phantom 3)

Figure 7 compares tomosynthesis slices reconstructed with SAA (figure 7a, c) and FBP (figure 7b, d), while figure 7e shows the image corresponding to the projection at 0^0 obtained in a PhC mode. On the same graph, plots of profiles taken horizontally across the ROIs (short arrows are shown) are presented.
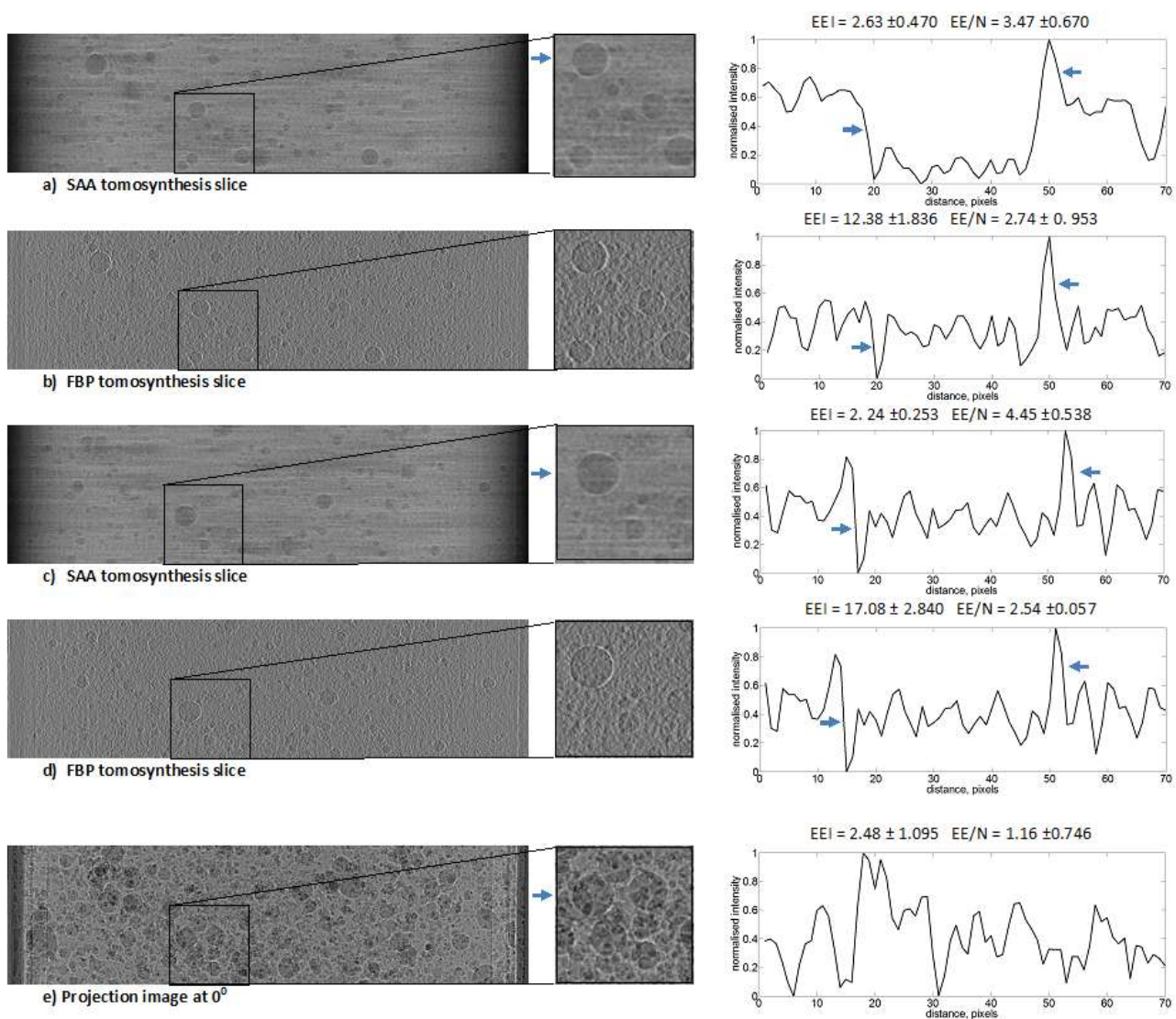
Figure 7: Comparison of PhC reconstructed tomosynthesis and planar images of the epoxy phantom (phantom 3) containing air sacs: selected tomosynthesis planes reconstructed with SAA (a, c) and FBP (b, d), respectively; (e) projection image corresponding to 0^0 (front view). The plotted profiles are taken horizontally across the largest spherical object in the ROI (short arrows are shown).

The edge enhancement effect observed in the projection image of this inhomogeneous phantom is well preserved in all tomosynthesis images. The superposition of internal details (air sacs) produces a texture background well visible in the projection view; on the other hand, reconstructed slices demonstrate partial removal of this complex background, showing fairly improved visibility for the details located in the corresponding plane, well defined object dimensions and location. This visual result is well supported by the quantitative evaluation of the images. The calculated EEI is much higher for slices, reconstructed by FBP, similarly to the evaluated cases of phantom 1 and phantom 2, which are characterised with homogeneous backgrounds.

This experimental test showed the potential of PhC tomosynthesis for resolving successfully the complexity of a highly structured background in the x-ray imaging of thick and inhomogeneous phantoms, at least in the case shown of high-contrast details.

III.B.2. Phantom 4

The results for phantom 4 are presented in figure 8 to 11. These figures show reconstructed features in four selected regions of interest (ROIs) contained in the BR3D commercial phantom: masses - ROI1 (figure 8), fibers - ROI2 and ROI3 (figures 9 and 10) and groups of microcalcifications - ROI4 (figure 11), for the PhC planar image and reconstructed FBP and SAA tomosynthesis images. Projection and reconstruction images appear mirrored compared to the annotation of the ROIs in figure1. As in the case of phantom 3, which is characterized by an inhomogeneous background, the simulated anatomical background, strongly present in the planar images (the top images in figures 8-11a-d) is removed in tomosynthesis images (second and third images in figures 8-11), thus leading to improved microcalcification and improved low-contrast visibility as well as edge sharpness of these features.
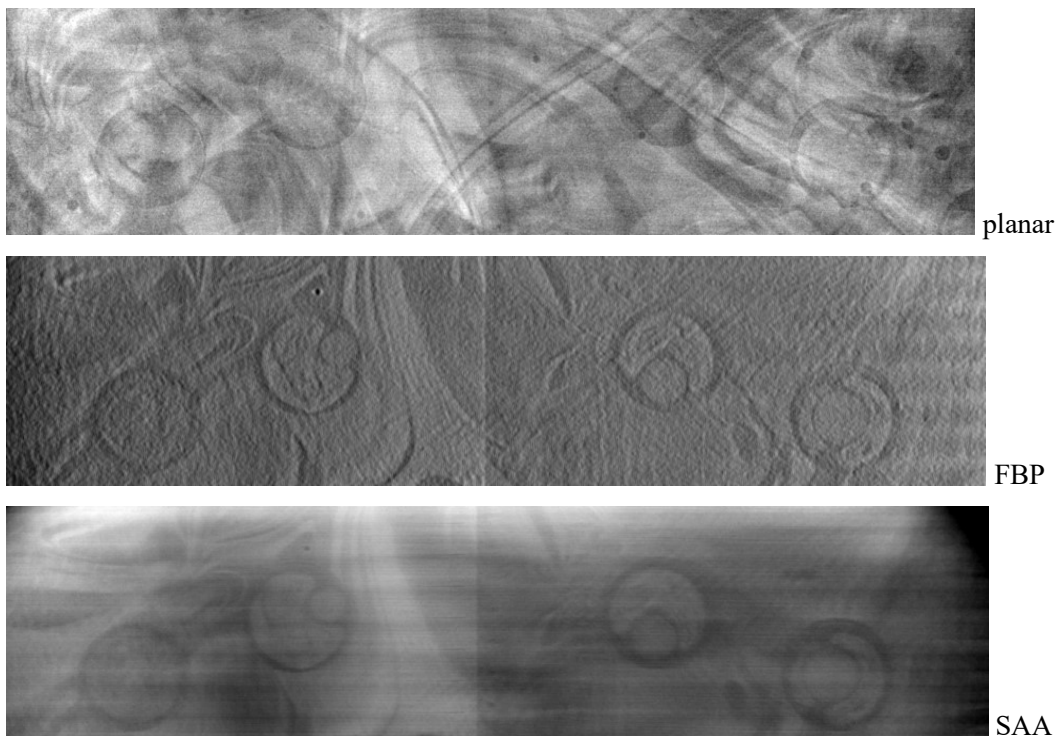

planar

FBP

SAA

Figure 8: Comparison of ROI1, containing low contrast details with size of 2.3mm, 3.1mm, 3.9mm and 4.7mm (from left to right), selected from the PhC planar image, FBP and SAA reconstructed tomosynthesis images of the BR3D phantom (phantom 4).
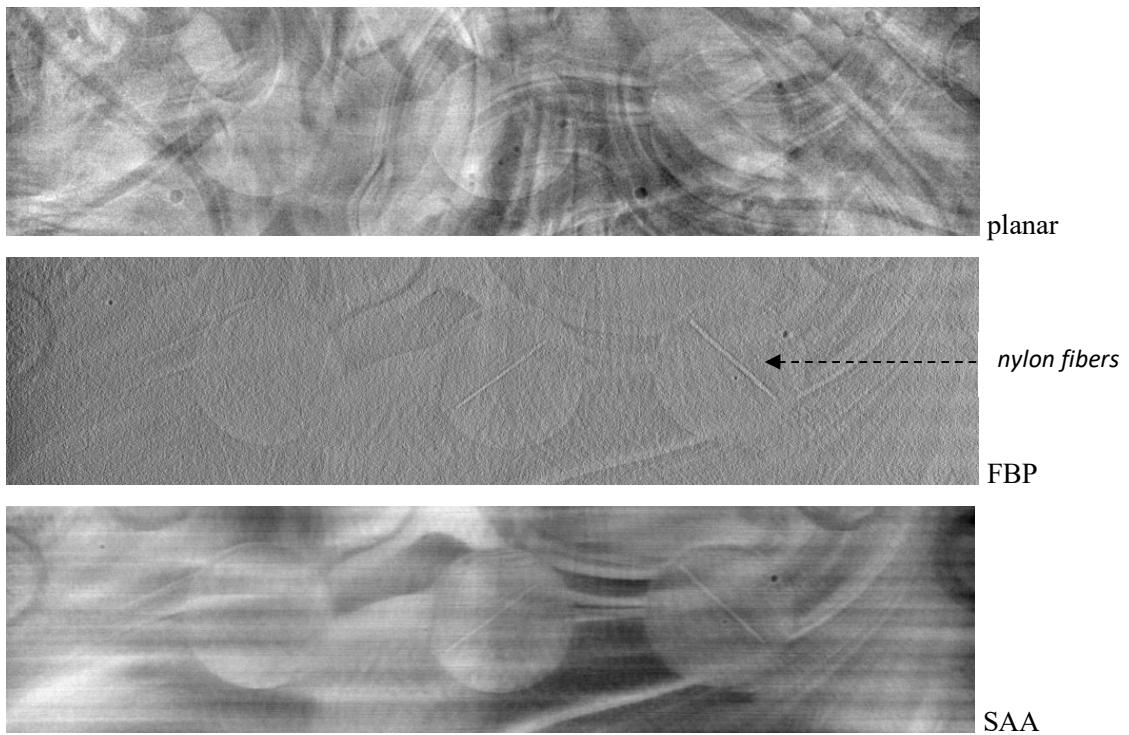
planar

nylon fibers

FBP

SAA

Figure 9: Comparison of ROI2, containing nylon fibers with diameters 0.12mm, 0.28mm and 0.41mm (from left to right), selected from the PhC planar image, FBP and SAA reconstructed tomosynthesis images of the BR3D phantom (phantom 4).

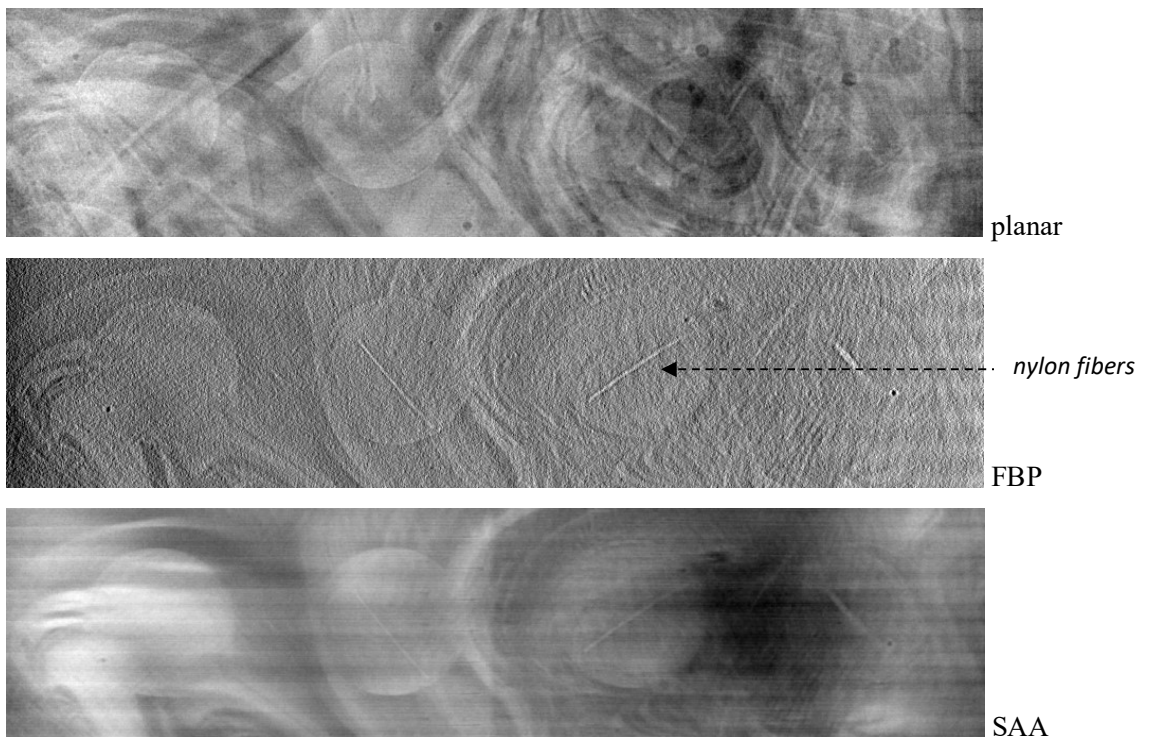planar

nylon fibers

FBP

SAA

Figure 10: Comparison of ROI3, containing nylon fibers with diameters 0.15mm, 0.23mm, 0.38mm and 0.60mm (from left to right), selected from the PhC planar image, FBP and SAA reconstructed tomosynthesis images of the BR3D phantom (phantom 4).
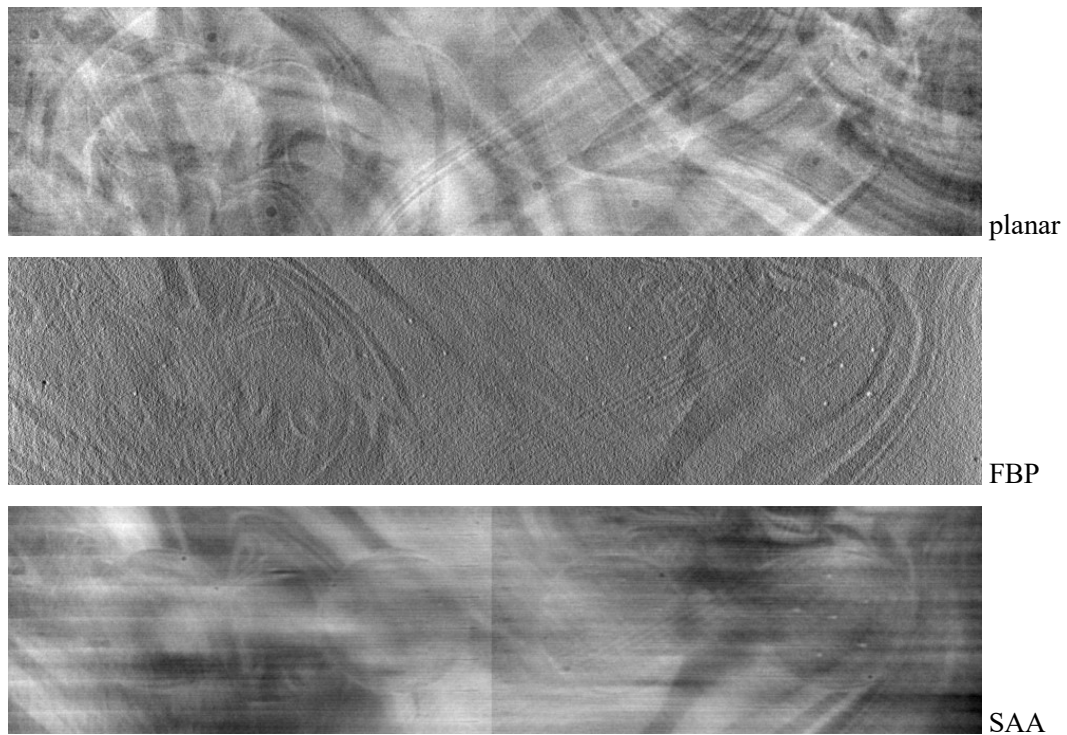
Figure 11: Comparison of ROI4, containing groups of microcalcifications of different size, selected from the PhC planar image, FBP and SAA reconstructed tomosynthesis images of the BR3D phantom (phantom 4).

The detailed comparison between the four ROIs taken from planar and tomosynthesis images, shown in figures 8 to 11, reveals that most detail features are visible only in tomosynthesis images (e.g., the groups of microcalcifications, the nylon fibers and the masses). For instance in ROI4 from the planar image (figure 11), only microcalcifications with a grain size of 0.400 mm may be seen; similarly, in reconstructed with SAA images this group of microcalcifications is also observed. By contrast, in FBP reconstructed images, microcalcifications with sizes between 0.196 mm and 0.400 mm are well visualised. For these details, contrast-to-noise ratio (CNR) and contrast were calculated and compared in table 2.

Table 2. Detail Contrast and Contrast to Noise Ratio for the four groups of microcalcifications, calculated on planar and reconstructed images.

modality	Parameter	microcalcification size			
		0.400mm	0.290mm	0.230mm	0.196mm
planar	CNR	2.76 ±0.682	-	-	-
	C,%	42.25 ± 10.443	-	-	-
SAA	CNR	4.45 ± 1.227	-	-	-
	C,%	1.02 ± 0.282	-	-	-
FBP	CNR	5.05 ± 0.666	5.02 ± 1.07	4.85 ± 0.503	2.97 ±0.408
	C,%	98.38 ± 12.978	93.87 ± 19.993	83.78 ±8.690	58.44 ±8.041

‑   not measured since the microcalcifications were not visible

CNR is higher for microcalcifications, reconstructed with FBP, as well as their contrast is much improved. This is explained with the high-frequency nature of the filter used to pre-process the projection images in the FBP, which gives rise to the high frequency content amplification. Similar results are reported from the task-based evaluation for the microcalcifications, summarised in table 3. Microcalcifications with size of 0.196 mm may be well seen on FBP images, while this is not the case for planar and SAA images.

Table 3. Results from the task-based evaluation applied for ROI 4 (groups of microcalcifications). In brackets, the number of microcalcifications seen per group is given.

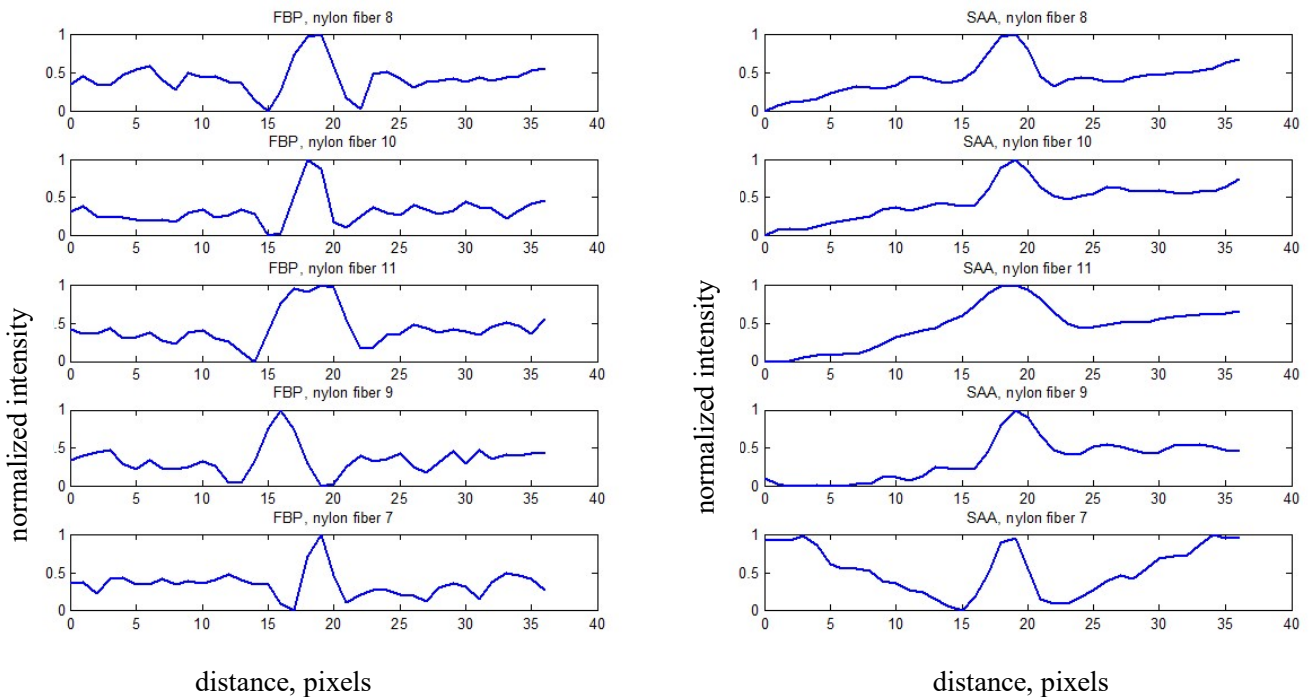| Modality	Observer	Group 1 0.196 mm	Group 2 0.230 mm	Group 3 0.290 mm	Group 4 0.400 mm	Ranking of the modality
Planar	1	1(0)	1(0)	1(0)	3(3)	3
	2	1(0)	1(0)	2(1)	3(6)	3
	3	2(1)	1(0)	3(4)	4(3)	3
FBP	1	2(2)	3(5)	4(6)	5(6)	1
	2	3(5)	4(6)	5(6)	5(6)	1
	3	3(6)	4(6)	5(6)	5(6)	1
SAA	1	1(0)	2(1)	2(1)	2(5)	2
	2	1(0)	1(1)	1(3)	5(6)	2
	3	1(0)	2(1)	2(3)	4(6)	2

Figure 12: Comparison of nylon fibers with diameters: fiber 7 – 0.6mm, fiber 8 –0.41mm, fiber 9 – 0.38mm, fiber 10 – 0.28mm, fiber 11- 0.23mm. ROI4 selected from the PhC planar image, the FBP and the SAA reconstructed PhC tomosynthesis images of the BR3D phantom (phantom 4).

Similar results were observed for the nylon fibers present in ROI2 and ROI3 (figures 9 and 10). From the nylon fibers, which have a length of 10 mm, the fibers with diameters in the range between 0.6 mm and 0.23 mm (ROI3) as well as 0.28 mm to 0.41 mm (ROI2) were slightly visible on projection images. On contrary, these fibers were well defined in both SAA and FBP reconstructed images. These fibers were not visible on the projection image mainly due to the inhomogeneous background containing tissue simulating materials with properties close to the absorption properties of real breast tissue. Line profiles were taken across these fibers and compared in figure 12. The comparison of the line profiles shows sharper edges of nylon fibers reconstructed with FBP in comparison with these reconstructed with SAA. This observation supports well the improved nylon fiber appearance in FBP images compared to SAA. The task-based evaluation, summarised in table 4, shows an advantage for the FBP, followed by the SAA and the planar images. Nylon fibers are almost invisible on planar images as the highest score in this case was 2, which corresponds to 'probably absent'. The observers noted that both the FBP and the SAA give similar results, however they preferred FBP due to the improved edge visibility.

Table 4. Results from the task-based evaluation applied for ROI 2-3 (nylon fibers).

Modality	Observer	Fibers 0.18 mm	Fibers 0.28 mm	Fibers 0.41 mm	Fibers 0.15 mm	Fibers 0.23 mm	Fibers 0.38 mm	Fibers 0.60 mm	Ranking of modality
Planar	1	1	1	1	1	2	1	1	3
	2	1	1	4	1	4	1	1	3
	3	1	1	2	1	2	2	2	3
FBP	1	1	5	5	1	5	5	3	1
	2	1	5	5	1	5	5	4	1
	3	2	5	5	3	3	5	5	1
SAA	1	1	3	4	1	3	4	3	2
	2	1	5	5	1	5	5	4	2
	3	1	5	5	1	5	5	5	2

Finally, masses are well visualised in both SAA and FBP tomosynthesis compared to masses in planar images. Indeed, masses in the planar image of ROI1 (figure 8) are not visible at all. These are hemispherical masses with size between 2.3mm and 4.7mm in diameter. Quantitatively, their CNR and contrast were evaluated and listed in table 5.

Table 5. Detail Contrast and Contrast to Noise Ratio for the four spheroidal masses, calculated on reconstructed images. Masses on planar images were not visible.

Modality	Parameter	Spheroidal Mass Size			
		2.3mm	3.1mm	3.9mm	4.7mm
SAA	CNR	1.60	16.92	0.76	1.21
	C,%	1.59	1.27	0.07	1.34
FBP	CNR	-	0.44	0.26	0.28
	C,%	-	49.39	58.56	40.92

- not measured since masses were not visible

As expected, masses reconstructed with SAA have higher CNR compared to FBP. This has already been demonstrated in a previous study at synchrotron facility (Bliznakova *et al.*, 2010). Random and structured noise in the images is related to the high-frequency components in the spectra of the images. SAA acts as a low-pass filter for the out-of-plane content, while the FBP preserves the whole content and this results in a lower CNR compared to SAA. The results from the quantitative assessment are well supported by the results of the task-based evaluation, summarized in table 6. The observers ranked the planar images on third place, while they evaluated the SAA to better reconstruct masses than the FBP. In addition, they all agree that low-contrast features were absent or probably absent on the planar image.

Table 6. Results from the task-based evaluation applied for ROI 1 (masses).

Modality	Observer	Mass 2.3 mm	Mass 3.1 mm	Mass 3.9 mm	Mass 4.3 mm	Ranking of modality
Planar	1	1	1	1	1	3
	2	1	1	1	3	3
	3	1	1	1	1	3
FBP	1	1	5	5	5	2
	2	1	5	5	5	2
	3	1	5	5	4	2
SAA	1	1	5	5	5	1
	2	3	5	5	5	1
	3	1	5	5	4	1

In overall, low contrast large area details, such as masses, are well reconstructed with SAA compared to FBP. The anatomical structured noise is fairly reduced and the masses are well visualized, despite the blurring effects, present on the image. In case of FBP, the in-plane and out-plane low frequency contain is suppressed. This combined with the high frequency noise in the reconstructed images leads to lower CNR values for the masses reconstructed by FBP in comparison to these reconstructed by SAA. Therefore, FBP combined with the Ram-Lak filter is a suitable algorithm for reconstructions of high contrast features like microcalcifications. In this case, the high frequency contain is amplified and at the same time the heterogeneous background is well suppressed, which results in higher CNR values for microcalcifications compared to these reconstructed with SAA.

Just as with x-ray projection mammography, PhC projection imaging lacks depth-of-focus information. When imaging thick, complex specimens (as in the case of phantom 3) or entire breast phantoms (as the case of phantom 4), the superposition of various features present in the sample complicates the image interpretation task. The use of 3D techniques, like digital tomosynthesis, overcomes at least in part these limitations. The current study showed the ability to improve the detection task: characterise precisely the location and dimensions of the objects within the phantom, as well as to preserve the edge enhancement that is observed in planar phase contrast projection images. The images shown were obtained with an in-line PhC setup. The in-line method is the

simplest and most adopted technique for PhC imaging, since it does not require the use, in the imaging setup, of any optics and grating elements between the sample and the detector, in order to perform wave splitting or any kind of image reconstruction.

The transfer of this imaging modality for breast imaging with monochromatic radiation to the clinical environment is being pioneered at the Elettra synchrotron facility (Trieste, Italy) (Arfelli *et al.*, 2000), with demonstration of higher contrast in PhC images than in the absorption images with synchrotron in the energy range of 15 keV and 25 keV, for breast tissue specimens. Preliminary results with patients examined on both synchrotron and conventional mammography units concluded that from the diagnostic point of view, the PhC synchrotron images were never inferior to those from conventional units (Dreossi *et al.*, 2007; Castelli *et al.*, 2007; Castelli *et al.*, 2011; Dreossi *et al.*, 2008). Recently at this infrastructure, a detail quantitative evaluation and optimization of phase-contrast CT has been accomplished in respect to the detection of small tumours in breast tissue (Gureyev *et al.*, 2014). In this framework, on the basis of the findings of this work, synchrotron digital breast tomosynthesis has potential for further improving the diagnostic task of lesion detection.

The experimental study was carried out at ID17 at ESRF, which beamline has at its disposal suitable large area detector. The closest possible distance between the detector and the object in PhC mode was approximately 6 m. Nowadays, this study could be successfully completed at the SYRMEP beamline at ELETTRA, for example at a distance of 166 cm (the longest available distance) and a large area detector. Recently, phase contrast CT was successfully applied at this beamline (Gureyev *et al.*, 2014). The authors evaluated both propagation-based and analyser-based PhC imaging combined with CT for two plastic phantoms and four excised breast samples. Appropriate conditions for realisation of this technique may be as well the medical beamline of the Australian Synchrotron, which owns large area detector and distance object-detector that could be adjusted up to 5m (Nesterets *et al.*, 2015).

In the present study, images were reconstructed by back-projection algorithms, which were already implemented in the reconstruction platform. However, these algorithms are characterised with some imperfections like streaking artifacts, shadowing around the dense reconstructed objects and other noise-like textures. These artifacts may obscure some of the fine anatomical details of the image. The last five years, efforts are being made at developing and modifying existing iterative reconstruction techniques applied to PhC images. Amongst these algorithms are the statistical iterative algorithm (Fahimian *et al.*, 2010; Hahn *et al.*, 2015), iterative based on Fourier transform (Cong *et al.*, 2012), algebraic reconstruction method (Fu *et al.*, 2015), iterative based on penalized maximum likelihood reconstruction algorithm (Brendel *et al.*, 2016). In all cases, the image quality is significantly improved in comparison to the FBP method. Therefore, a continuation of this work will concern the realisation of iterative algorithms and use with the available image sets. It is also planned these algorithms to be applied using projections obtained from in-house developed anthropomorphic breast phantoms (Bliznakova *et al.*, 2016) and breast tissue samples.

For the setup at beamline ID17 at ESRF, the time for obtaining an image with a height of 6mm and width of 150 mm was 26 ms. For an image with a height of 18 cm, the needed time for exposure for 17 images in a tomosynthesis arc will be 13.26 s, which is almost double compared to conventional breast tomosynthesis (Qian *et al.*, 2012). In these calculations, the time needed for the platform movement in z direction has not been taken into account. The needed time would depend on the used setup, detector size and properties and it is also a subject to optimisation, since the number of images may be decreased and the resolution of the detector could be lower than the used in the study.

IV.   Conclusions

The SAA and FBP algorithms were successfully tested for PhC tomosynthesis. This experimental phantom study showed that features were well differentiated and characterized on tomosynthesis images. In addition, their edges are still sharp, similarly to the planar case. It is important that PhC tomosynthesis was capable of preserving enhanced edges in the reconstructed images especially for thick and inhomogeneous phantoms. Edge visibility is much improved when using FBP, which results in a much better subjective (visual) determining of the contours of the details of interest. However, images reconstructed with SAA look more similar to the classic tomographic images and provide a better perception for the reconstructed tissues. In this sense, the two reconstruction algorithms can be considered as complementary reconstruction techniques for evaluating more complex phantoms. In a clinical perspective, in-line PhC breast tomosynthesis might improve the task of detection of suspicious areas in the mammography images by adding the edge enhancement effect (due to phase contrast), to the reconstructed attenuation images. Further investigations will be devoted to the validation of the presented findings by imaging *ex vivo* breast samples and elaboration of the current SAA and FBP algorithms to improve the reconstructions of objects from PhC images.

Conflict of Interest Statement

None declared.

References:

Arfelli F, Bonvicini V, Bravin A, Cantatore G, Castelli E, Palma L D, Michiel M D, Fabrizioli M, Longo R, Menk R H, Olivo A, Pani S, Pontoni D, Poropat P, Prest M, Rashevsky A, Ratti M, Rigon L, Tromba G, Vacchi A, Vallazza E and Zanconati F 2000 Mammography with synchrotron radiation: phase-detection techniques *Radiology* **215** 286-93

Berger M J, Hubbell J H, Seltzer S M, Chang J, Coursey J S, Sukumar R, Zucker D S and Olsen K 2010 XCOM: Photon Cross Section Database (version 1.5). In: *[Online] Available: http://physics.nist.gov/xcom [Saturday, 26-Jul-2014 05:42:53 EDT]. National Institute of Standards and Technology, Gaithersburg, MD.,*

Bliznakova K, Kolitsi Z, Speller R D, Horrocks J A, Tromba G and Pallikarakis N 2010 Evaluation of digital breast tomosynthesis reconstruction algorithms using synchrotron radiation in standard geometry *Medical physics* **37** 1893-903

Bliznakova K, Mettivier G, Russo P and Buliev I 2016 Contrast detail phantoms for X-ray phase-contrast mammography and tomography, *IWDM Malmo, June 18-22, 2016, Springer International Publishing Switzerland 2016*

Bliznakova K, Russo P, Mettivier G, Requardt H, Popov P, Bravin A and Buliev A 2015 A software platform for phase contrast x-ray breast imaging research *Computers in biology and medicine* **61** 62-74

Bravin A, Mocella V, Coan P, Astolfo A and Ferrero C 2007 A numerical wave-optical approach for the simulation of analyzer-based x-ray imaging *Optics express* **15** 5641-8

Brendel B, von Teuffenbach M, Noel P B, Pfeiffer F and Koehler T 2016 Penalized maximum likelihood reconstruction for x-ray differential phase-contrast tomography *Medical physics* **43** 188-94

Castelli E, Arfelli F, Dreossi D, Longo R, Rokvic T, Cova M A, Quaia E, Tonutti M, Zanconati F, Abrami A, Chenda V, Menk R H, Quai E, Tromba G, Bregant P and de Guarrini F 2007 Clinical mammography at the SYRMEP beam line *Nucl Instrum Meth A* **572** 237-40

Castelli E, Tonutti M, Arfelli F, Longo R, Quaia E, Rigon L, Sanabor D, Zanconati F, Dreossi D, Abrami A, Quai E, Bregant P, Casarin K, Chenda V, Menk R H, Rokvic T, Vascotto A, Tromba G and Cova M A 2011 Mammography with Synchrotron Radiation: First Clinical Experience with Phase-Detection Technique *Radiology* **259** 684-94

CIRS BR3D breast imaging phantom.

Cong W X, Momose A and Wang G 2012 Fourier transform-based iterative method for differential phase-contrast computed tomography *Optics letters* **37** 1784-6

Donnelly E F, Lewis K G, Wolske K M, Pickens D R and Price R R 2006 Characterization of the phase-contrast radiography edge-enhancement effect in a cabinet x-ray system *Physics in medicine and biology* **51** 21-30

Dreossi D, Abrami A, Arfelli F, Bregant R, Casarin K, Chenda V, Cova M A, Longo R, Menk R H, Quai E, Quaia E, Rigon L, Rokvic T, Sanabor D, Tonutti M, Tromba G, Vascotto A, Zanconati F and Castelli E 2008 The mammography project at the SYRMEP beamline *European journal of radiology* **68** S58-S62

Dreossi D, Bergamaschi A, Schmitt B, Vallazza E, Arfelli F, Longo R, Menk R H, Rigon L, Rokvic T, Venanzi C and Castelli E 2007 Clinical mammography at the SYRMEP beam line: Toward the digital detection system *Nucl Instrum Meth A* **576** 160-3

Durand M A, Haas B M, Yao X, Geisel J L, Raghu M, Hooley R J, Horvath L J and Philpotts L E 2015 Early clinical experience with digital breast tomosynthesis for screening mammography *Radiology* **274** 85-92

Fahimian B P, Mao Y, Cloetens P and Miao J W 2010 Low-dose x-ray phase-contrast and absorption CT using equally sloped tomography *Phys Med Biol* **55** 5383-400

Friedewald S M, Rafferty E A and Conant E F 2014 Breast cancer screening with tomosynthesis and digital mammography-reply *JAMA : the journal of the American Medical Association* **312** 1695-6

Fu J, Hu X H, Velroyen A, Bech M, Jiang M and Pfeiffer F 2015 3D Algebraic Iterative Reconstruction for Cone-Beam X-Ray Differential Phase-Contrast Computed Tomography *PloS one* **10**

Guan H, Xu Q, Garson A and Anastasio M A *Medical Imaging 2014: Physics of Medical Imaging, (San Diego, CA, 2014a),* vol. Series 9033*)*: SPIE)

Guan H F, Xu Q F, Garson A and Anastasio M A 2014b Depth resolution properties of in-line X-ray phase-contrast tomosynthesis *Medical Imaging 2014: Physics of Medical Imaging* **9033**

Gureyev T E, Mayo S C, Nesterets Y I, Mohammadi S, Lockie D, Menk R H, Arfelli F, Pavlov K M, Kitchen M J, Zanconati F, Dullin C and Tromba G 2014 Investigation of the imaging quality of synchrotron-based phase-contrast mammographic tomography *J Phys D Appl Phys* **47**

Hahn D, Thibault P, Fehringer A, Bech M, Koehler T, Pfeiffer F and Noel P B 2015 Statistical iterative reconstruction algorithm for X-ray phase-contrast CT *Scientific reports* **5**

Hammonds J C, Price R R, Donnelly E F and Pickens D R 2011 Phase-contrast digital tomosynthesis *Medical physics* **38** 2353-8

Ikeya A, Teramoto A, Noguchi K and Fujita H *Medical Imaging 2013: Physics of Medical Imaging, (Lake Buena Vista, FL, 2013),* vol. Series 8668*)*

Kamarianakis Z, Buliev I and Pallikarakis N 2013 A C++ platform for Image Reconstruction in X-ray Imaging. In: *5th Panhellenic Conference on Biomedical Technologies, ELEVIT,* (Athens, Greece

Kamarianakis Z, Buliev I and Pallikarakis N 2014 A platform for image reconstruction in X-ray imaging: Medical applications using CBCT and DTS algorithms *CSJM* **22** 236-52

Kolitsi Z, Panayiotakis G, Anastassopoulos V, Scodras A and Pallikarakis N 1992 A multiple projection method for digital tomosynthesis *Medical physics* **19** 1045-50

Kopans D B 2014 Digital breast tomosynthesis from concept to clinical care *AJR. American journal of roentgenology* **202** 299-308

Li K, Ge Y, Garrett J, Bevins N, Zambelli J and Chen G H 2014 Grating-based phase contrast tomosynthesis imaging: Proof-of-concept experimental studies *Medical physics* **41**

Nesterets Y I, Gureyev T E, Mayo S C, Stevenson A W, Thompson D, Brown J M C, Kitchen M J, Pavlov K M, Lockie D, Brun F and Tromba G 2015 A feasibility study of X-ray phase-contrast mammographic tomography at the Imaging and Medical beamline of the Australian Synchrotron *J Synchrotron Radiat* **22** 1509-23

Qian X, Tucker A, Gidcumb E, Shan J, Yang G, Calderon-Colon X, Sultana S, Lu J, Zhou O, Spronk D, Sprenger F, Zhang Y, Kennedy D, Farbizio T and Jing Z 2012 High resolution stationary digital breast tomosynthesis using distributed carbon nanotube x-ray source array *Medical physics* **39** 2090-9

Sarkar V, Shi C, Rassiah-Szegedi P, Diaz A, Eng T and Papanikolaou N 2009 The effect of a limited number of projections and reconstruction algorithms on the image quality of megavoltage digital tomosynthesis *Journal of applied clinical medical physics / American College of Medical Physics* **10** 2970

Sarno A, Mettivier G and Russo P 2015 Dedicated breast computed tomography: Basic aspects *Medical physics* **42** 2786-804

Schleede S, Bech M, Grandl S, Sztrókay A, Herzen J, Mayr D, Stockmar M, Potdevin G, Zanette I, Rack A, Weitkamp T and Pfeiffer F 2014 X-ray phase-contrast tomosynthesis for improved breast tissue discrimination *European journal of radiology* **83** 531-6

Sechopoulos I 2013 A review of breast tomosynthesis. Part I. The image acquisition process *Medical physics* **40** 014301

Szafraniec M B, Millard T P, Ignatyev K, Speller R D and Olivo A 2014 Proof-of-concept demonstration of edge-illumination x-ray phase contrast imaging combined with tomosynthesis *Phys Med Biol* **59** N1-N10